



Quantitative evaluation of LDDMM, FreeSurfer, and CARET for cortical surface mapping

Jidan Zhong^a, Desiree Yee Ling Phua^d, Anqi Qiu^{a,b,c,d,*}

^a NUS Graduate School for Integrative Sciences and Engineering, National University of Singapore, Singapore, Singapore

^b Division of Bioengineering, National University of Singapore, Singapore, Singapore

^c Clinical Imaging Research Center, National University of Singapore, Singapore, Singapore

^d Singapore Institute for Clinical Sciences, the Agency for Science, Technology and Research, Singapore, Singapore

ARTICLE INFO

Article history:

Received 2 February 2010

Revised 27 March 2010

Accepted 31 March 2010

Available online 8 April 2010

Keywords:

Diffeomorphic metric mapping

Laplace-Beltrami operator

Curve variation

Surface alignment consistency

ABSTRACT

Cortical surface mapping has been widely used to compensate for individual variability of cortical shape and topology in anatomical and functional studies. While many surface mapping methods were proposed based on landmarks, curves, spherical or native cortical coordinates, few studies have extensively and quantitatively evaluated surface mapping methods across different methodologies. In this study we compared five cortical surface mapping algorithms, including large deformation diffeomorphic metric mapping (LDDMM) for curves (LDDMM-curve), for surfaces (LDDMM-surface), multi-manifold LDDMM (MM-LDDMM), FreeSurfer, and CARET, using 40 MRI scans and 10 simulated datasets. We computed curve variation errors and surface alignment consistency for assessing the mapping accuracy of local cortical features (e.g., gyral/sulcal curves and sulcal regions) and the curvature correlation for measuring the mapping accuracy in terms of overall cortical shape. In addition, the simulated datasets facilitated the investigation of mapping error distribution over the cortical surface when the MM-LDDMM, FreeSurfer, and CARET mapping algorithms were applied. Our results revealed that the LDDMM-curve, MM-LDDMM, and CARET approaches best aligned the local curve features with their own curves. The MM-LDDMM approach was also found to be the best in aligning the local regions and cortical folding patterns (e.g., curvature) as compared to the other mapping approaches. The simulation experiment showed that the MM-LDDMM mapping yielded less local and global deformation errors than the CARET and FreeSurfer mappings.

© 2010 Elsevier Inc. All rights reserved.

Introduction

The human cortex is a convoluted sheet that forms sulco-gyral folding patterns to allow for a large surface area inside the skull. Because of this, functionally distinct regions are close to each other in a volume space but geometrically distant in terms of distance measured along the cortex. Such geometric property of the cortex has been preserved well in the cortical surface model (Van Essen et al., 1998; Fischl et al., 1999a; Van Essen, 2004a; Clouchoux et al., 2005; Lyttelton et al., 2007). Thus, researchers have recently focused on developing techniques for cortical parcellation, cortical morphological and functional studies using the cortical surface model (Fischl and Dale, 2000; Fischl et al., 2004; Anticevic et al., 2008). In particular, registration for the cortical surface has received great attention in both anatomical and functional studies in magnetic resonance imaging (MRI) (Van Essen et al., 1998; Fischl et al., 1999a; Van Essen, 2004a; Clouchoux et al., 2005; Lyttelton et al., 2007). It has been widely applied in

brain morphometric studies not only for exploring abnormalities in the cortical morphology and functions associated with disease but also for providing the locations (e.g., Sowell et al., 2003; Chung et al., 2005; Narr et al., 2007). Moreover, functional studies have shown that cortical surface mappings have superior power in detecting functional activations as compared to automated Talairach registration (Fischl et al., 1999b) and affine volume-based registration approaches (Anticevic et al., 2008).

Since the cortex is highly folded, its surface representation has been suggested to facilitate the visualization and analysis of functional data by preserving its important geometrical and topological relationships. One well-known representation is the sphere. Various methods have been proposed to inflate the cortical surface and then project it onto a unit sphere, such as CARET (Van Essen, 2005), FreeSurfer (Fischl et al., 1999a), conformal mappings (Gu et al., 2004; Hurdal and Stephenson, 2004). Thus, a majority of early cortical surface mapping approaches were developed in the spherical coordinates where landmarks (e.g., points or gyral/sulcal curves) or cortical folding patterns were driving forces to align one cortical sphere to the other (Thompson and Toga, 1996; Fischl et al., 1999a; Robbins et al., 2004; Van Essen, 2004b, 2005; Yeo et al., 2009). Among them, curve-based CARET and folding-pattern-based FreeSurfer cortical mapping

* Corresponding author. Division of Bioengineering, National University of Singapore, 9 Engineering Drive 1, Block EA #03-12, Singapore 117576, Singapore. Fax: +65 6872 3069.

E-mail address: bieqa@nus.edu.sg (A. Qiu).

algorithms have been widely used partly because they are publicly available and provide reasonable cortical alignments. Nevertheless, the curve or folding-pattern-based spherical mappings require the spherical parameterization of the cortical surface in which adjacent gyri with distinct functions are well separated. This surface parameterization process introduces distance, area, and angular distortions that potentially affect the quality of the surface alignment. To avoid such an issue, one would expect to directly align the cortical surfaces in their own coordinates. In 2005, Vaillant and Glaunès (Vaillant and Glaunès, 2005) first introduced a vector-valued measure acting on vector fields as geometric representation of surfaces in their own space and then imposed a Hilbert space structure on it, whose norm was used to quantify the geometric similarity between two surfaces in their own coordinates. Since then, the vector-valued measure has been incorporated as a matching functional in the variational problems of large deformation diffeomorphic metric surface mapping (LDDMM) (Vaillant and Glaunès, 2005; Vaillant et al., 2007). Following this work, several LDDMM algorithms have been developed to map gyral/sulcal curves (LDDMM-curve) (Qiu and Miller, 2007; Glaunès et al., 2008) and simultaneously align cortical surfaces and gyral/sulcal curves (multi-manifold LDDMM, MM-LDDMM) (Zhong and Qiu, 2010). Several studies have shown the robustness of the LDDMM algorithms in registering cortical surfaces using curves (Qiu and Miller, 2007) or both curves and surfaces (Zhong and Qiu, 2010).

While many cortical mapping approaches are available, anatomical and functional studies have suggested that different mapping algorithms can influence statistical outcomes in group analysis (Desai et al., 2005; Qiu et al., 2007). Thus, it is important to know the performance of each mapping algorithm, especially in regions of interests (ROIs), to properly interpret image findings. To our knowledge, no study has directly compared the LDDMM approaches with spherical registration methods, such as those in CARET and FreeSurfer, to address their mapping accuracies. In this paper, we aim to quantitatively compare these cortical surface mapping algorithms, including LDDMM-curve, LDDMM-surface, MM-LDDMM, FreeSurfer, and CARET in terms of registration accuracy for local (gyral/sulcal curves and sulcal regions) and global (folding pattern) cortical features. In addition, we conducted a simulation experiment to evaluate mapping error distribution over the cortical surface and localize regions with large mapping errors for each mapping algorithm, which potentially provides guidance for the choice of mapping algorithms in ROI-specific imaging studies.

Methods

Subjects and image acquisition

Forty subjects comprising of 10 young adults (five males and five females, age: 23.4 ± 2.55 years), 10 middle-aged adults (five males and five females, age: 49.3 ± 1.89 years), 10 elderly (five males and five females, age: 73.9 ± 2.02 years), and 10 patients with Alzheimer's disease (five males and five females, age: 76.4 ± 2.55 years) were randomly selected from the OASIS database (Marcus et al., 2007). An average atlas was not used in this study because mapping accuracy may be biased to the mapping algorithm that was applied to generate the average atlas. Thus, a single-subject template was constructed using an MRI scan collected from a healthy subject (female, age: 54 years). This subject was chosen because her age and total brain volume were at the average values of the 40 subjects in this study.

Magnetic resonance (MR) scans for the whole brain were acquired using the Siemens Magnetom Vision 1.5 T imaging system using Magnetization Prepared Rapid Gradient Recalled Echo (MP-RAGE) sequence (TR = 9.7 ms, TE = 4 ms, flip angle = 10° , inversion time (TI) = 20 ms, delay time (TD) = 200 ms, 256×256 (1×1 mm) in-plane resolution, 128 1.25-mm slices without gaps). Three or four T1-weighted MP-RAGE scans were collected for each subject. Head movement was minimized by cushioning and a thermoplastic face

mask. All MR images used in this study are accessible online (<http://www.oasis-brains.org>) (Marcus et al., 2007).

Cortical surface generation

The three or four MP-RAGE data per subject were averaged offline (with correction for head movement) to increase the contrast to noise ratio and were interpolated into isotropic voxels with resolution of $1 \text{ mm} \times 1 \text{ mm} \times 1 \text{ mm}$. FreeSurfer was used to label each voxel as cerebrospinal fluid (CSF), gray matter (GM), and white matter (WM) using a Markov-Random field model (Fischl et al., 2002). An inner surface at the boundary of GM and WM was constructed and then propagated to the boundary of GM and CSF to form an outer surface via a flow with the force based on the image labeling and gradient such that the topologies of the outer and inner surfaces were preserved (Dale et al., 1999). The fiducial surface, the center of the inner and outer surfaces, was then smoothed by changing the location of each vertex toward the barycenter of its first neighbors to reduce noise features and small geometric changes of shapes (Toro and Burnod, 2003). For the rest of the paper, this smoothed fiducial surface was considered as geometric representation of the cortex and used as input surface for LDDMM, FreeSurfer, and CARET cortical surface mappings. Examples of the cortical surface are illustrated in the first column of Fig. 1.

Cortical surface mapping algorithms

LDDMM

Two cortical surfaces may be mapped onto each other by treating the two-dimensional manifolds of the cortical surfaces as one-dimensional features (curves), or two-dimensional structure of the manifold as a whole, or combination of one- and two-dimensional features (curves and surface). Compared to two-dimensional surface matching, an advantage of one-dimensional curve mapping is that the amount of computation is reduced. Also, the selection of curves can be guided by previous knowledge derived from postmortem studies. In the setting of LDDMM, we developed mapping algorithms that utilize three different anatomical manifolds, i.e., curves (Qiu and Miller, 2007; Glaunès et al., 2008), surfaces (Vaillant and Glaunès, 2005; Vaillant et al., 2007), and integration of curves and surfaces (Zhong and Qiu, 2010). All of these mapping algorithms provide diffeomorphic maps (i.e., one-to-one, reversible smooth transformations that preserve topology) that allow deforming one cortical surface to a template in its own folded coordinates. The use of LDDMM for mapping the cortical surfaces requires studying them in a metric space, provides a diffeomorphic transformation, and defines a metric distance that can be used to quantify the similarity between two shapes. We assume that shape objects can be generated one from the other via a flow of diffeomorphisms, solutions of ordinary differential equation $\dot{\phi}_t = v_t(\phi_t)$, $t \in [0, 1]$ with $\phi_0 = id$, identity map, and associated velocity fields v_t . For a pair of objects I_{temp} and I_{targ} , a diffeomorphic map φ transforms one to the other $\phi_1 \cdot I_{temp} = I_{targ}$ at time $t = 1$. We defined a variational problem to find optimal transformation, ϕ_t , $t \in [0, 1]$ in the form of

$$J(v_t) = \inf_{v_t: \dot{\phi}_t = v_t(\phi_t), \phi_0 = id} \int_0^1 \|v_t\|_V^2 dt + E(\phi_1 \cdot I_{temp}, I_{targ}), \quad (1)$$

where the first term quantifies the metric distance between the shapes, the length of the geodesic curves $\phi_t \cdot I_{temp}$, $t \in [0, 1]$ through the shape space generated from connecting I_{temp} to I_{targ} in a Hilbert space, V , of smooth vector fields with norm $\|\cdot\|_V$. V ensures that the solutions are diffeomorphisms. $E(\phi_1 \cdot I_{temp}, I_{targ})$ quantifies the closeness between the deformed object $\phi_1 \cdot I_{temp}$ and object I_{targ} . We adapted this variational problem to different objects, such as curves (Qiu and Miller, 2007; Glaunès et al., 2008), surfaces (Vaillant and Glaunès, 2005; Vaillant et al., 2007), and integration of curves and surfaces (Zhong and Qiu, 2010). For the purpose of registering two cortical surfaces, we briefly reviewed

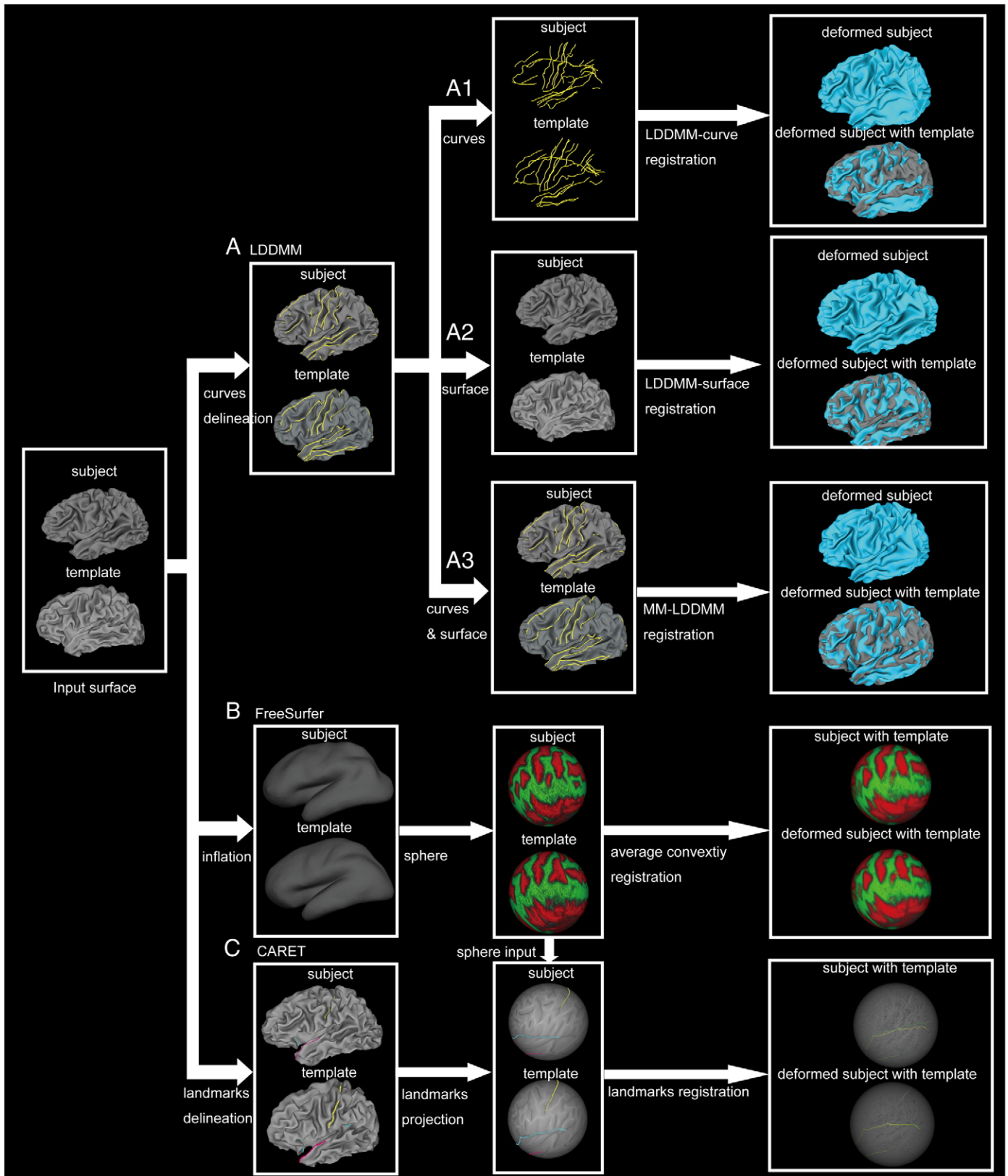


Fig. 1. Schematic of LDDMM, FreeSurfer, and CARET cortical mapping processing pipelines.

how to define $E(\phi_1 \cdot I_{\text{temp}}, I_{\text{targ}})$ for objects of curves, surfaces, and integration of curves and surfaces.

LDDMM-curve. Since a curve is a geometric object, it cannot be uniquely reconstructed based on the locations of a set of points. We consider a

curve embedded in R^3 as a one-dimensional manifold in the sense that the local region of every point on the curve is equivalent to a line which can be uniquely defined by this point and the tangent vector at this location. Thus, we represent our mapping object, I , as $I = \{\gamma^i, i = 1, 2, \dots, n_c\}$, where $\{\gamma^i\}_{i=1}^{n_c}$ is a set of gyral and sulcal curves on the surface associated with a

series of points and their tangent vectors. n_c is the total number of paired curves. We defined $E(\phi_1 \cdot I_{\text{temp}}, I_{\text{targ}})$ in Eq. (1) as

$$E(\phi_1 \cdot I_{\text{temp}}, I_{\text{targ}}) = \sum_{i=1}^{n_c} E_{\gamma_i}(\phi_1 \cdot \gamma_{\text{temp}}^i, \gamma_{\text{targ}}^i),$$

where $\phi_1 \cdot \gamma_{\text{temp}}^i$ is the deformed template curve while γ_{targ}^i is the target curve. $E_{\gamma_i}(\phi_1 \cdot \gamma_{\text{temp}}^i, \gamma_{\text{targ}}^i)$ quantifies the closeness of the i^{th} paired curves $\phi_1 \cdot \gamma_{\text{temp}}^i$ and γ_{targ}^i by computing the similarity of the tangent vectors of these two curves.

As illustrated in Fig. 2, 14 sulcal and 12 gyral curves were semi-automatically delineated for each subject and subsequently used for the LDDMM-curve mapping in this study. These curves were chosen because they are consistently present and readily identifiable on the cortex. The anatomical definitions of these curves are described elsewhere (Zhong and Qiu, 2010) (<http://www.bioeng.nus.edu.sg/cfa/mapping/curveprotocol.html>). Briefly, the initial starting and ending points of each curve were manually defined on the fiducial surface and the gyral (or sulcal) curve between them was automatically generated using dynamic programming by maximizing (or minimizing) the curvature information along the curve (Ratnanather et al., 2003). In this study, we deformed the fiducial surface of each individual subject to the template surface by interpolating the deformation field obtained from the LDDMM-curve algorithm via the diffeomorphic flow.

LDDMM-surface. We assume the cortical surface embedded in R^3 to be a two-dimensional manifold in the sense that the neighborhood of every point on the surface is equivalent to a two-dimensional plane in Euclidean space. Such a plane can be uniquely defined by a point and a vector originated at this point and normal to the plane. Next, we defined $E(\phi_1 \cdot I_{\text{temp}}, I_{\text{targ}})$ for registering surfaces in the LDDMM setting based on their position and normal vectors, in which $E(\phi_1 \cdot I_{\text{temp}}, I_{\text{targ}})$ in Eq. (1), is given in the form of

$$E(\phi_1 \cdot I_{\text{temp}}, I_{\text{targ}}) = E_S(\phi_1 \cdot S_{\text{temp}}, S_{\text{targ}}),$$

where $E_S(\phi_1 \cdot S_{\text{temp}}, S_{\text{targ}})$ quantifies the closeness of the deformed template and target surfaces by computing the similarity of their normal vectors. In our study, the LDDMM-surface algorithm was used to deform the fiducial surface of each individual subject to the template surface.

MM-LDDMM. We assume the cortical surface embedded in R^3 to be a multi-manifold, integration of one- and two-dimensional manifolds (curves and surfaces). Multi-manifold large deformation diffeomorphic metric mapping (MM-LDDMM) (Zhong and Qiu, 2010) was designed to integrate the gyral/sulcal curves and the fiducial surface together and thus allowed carrying the cortical surface and its gyral/sulcal curves simultaneously from one to the other through a flow of diffeomorphisms. MM-LDDMM incorporates anatomical priors through gyral and sulcal curves to constrain regional alignment, and the geometry of the fiducial surface to constrain regional and global alignment. Thus, we represent our mapping object, I , as $I = \{S, \gamma^i, i = 1, 2, \dots, n_c\}$, where S is the fiducial surface associated with a set of vertices and their normal vectors. $\{\gamma^i\}_{i=1}^{n_c}$ is a set of gyral and sulcal curves on the surface associated with a series of points and their tangent vectors. In the MM-LDDMM setting, we define $E(\phi_1 \cdot I_{\text{temp}}, I_{\text{targ}})$ for aligning the fiducial surface as well as sulcal and gyral curves in the form of

$$E(\phi_1 \cdot I_{\text{temp}}, I_{\text{targ}}) = E_S(\phi_1 \cdot S_{\text{temp}}, S_{\text{targ}}) + \sum_{i=1}^{n_c} E_{\gamma_i}(\phi_1 \cdot \gamma_{\text{temp}}^i, \gamma_{\text{targ}}^i),$$

where $E_{\gamma_i}(\phi_1 \cdot \gamma_{\text{temp}}^i, \gamma_{\text{targ}}^i)$ and $E_S(\phi_1 \cdot S_{\text{temp}}, S_{\text{targ}})$ are described previously. In our study, the fiducial surface of each individual subject was deformed to the template surface using the MM-LDDMM algorithm where the fiducial surface in the LDDMM-surface algorithm as well as the 14 sulcal and 12 gyral curves in the LDDMM-curve algorithm were considered as mapping objects.

FreeSurfer cortical mapping

Unlike LDDMM approaches, the cortical mapping algorithm in FreeSurfer requires spherical parameterization of the cortical surface

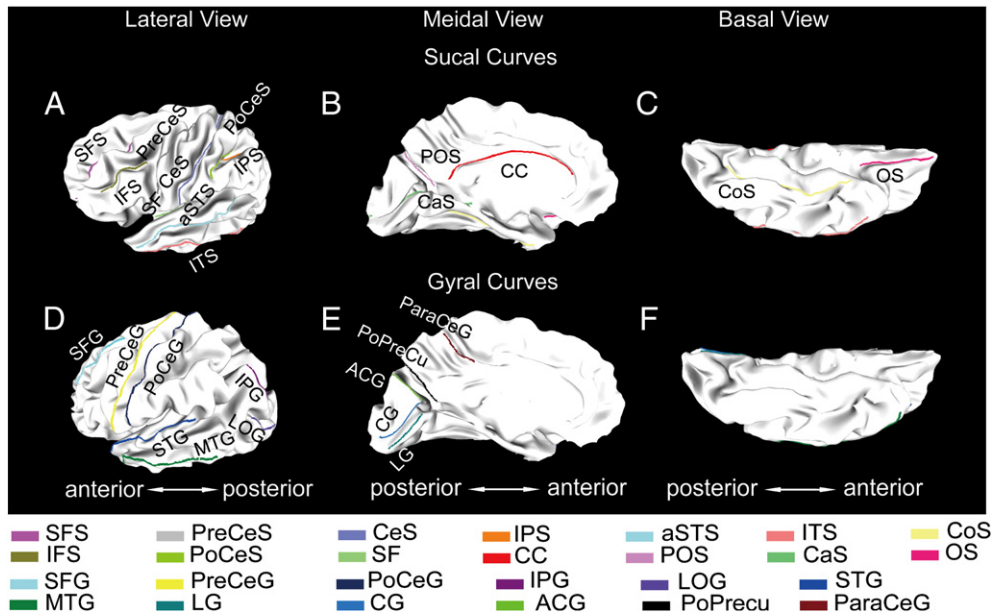


Fig. 2. Fourteen sulcal curves and 12 gyral curves are illustrated in the lateral (panels A, D), medial (panels B, E), and basal (panels C, F) views of the template surface. The top and bottom rows show sulcal and gyral curves respectively. Key: Panel (A): SFS(1), superior frontal sulcus; IFS(2), inferior frontal sulcus; PreCeS(3), precentral sulcus; CeS(23), central sulcus; PoCeS(4), postcentral sulcus; IPS(5), intraparietal sulcus; SF(6), Sylvian fissure; aSTS(7), anterior segment of the superior temporal sulcus; ITS(8), inferior temporal sulcus. Panel (B): CC(24), superior callosal sulcus; POS(9), parieto-occipital sulcus; CaS(25), calcarine sulcus. Panel (C): OS(10), olfactory sulcus; CoS(11), collateral sulcus. Panel (D): PreCeG(12), precentral gyrus; PoCeG(13), postcentral gyrus; STG(26), superior temporal gyrus; MTG(14), middle temporal gyrus; IPG(15), intraparietal gyrus; SFG(20), superior frontal gyrus; LOG(22), lateral occipital gyrus. Panel (E): LG(16), lingual gyrus; CG(17), cuneus gyurs; ACG(18), anterior border of the cuneus gyrus; PoPreCu(19), posterior border of the precuneus; ParaCeG(21), paracentral gyrus.

and then aligns cortical patterns (e.g., cortical convexity, cortical curvature) in the spherical coordinates. For these, Fischl and colleagues proposed several variational problems for cortical inflation, and spherical mapping (Fischl et al., 1999a,b). As illustrated in Fig. 1(B), the folded cortical surface was first inflated to remove its intrinsic folding pattern while minimizing metric distortion and a spring force that constrained the smoothness of the surface. Thus, the cortical inflation provided a representation of the cortical hemisphere that retained much of the shape and metric properties of the original surface, yet allowing for better visualization of functional activity occurring within sulci. The inflated surface was then projected onto a unit sphere by moving each vertex in the tessellation of the inflated surface to the closest point on the sphere based on surface normal vector. The metric distortion introduced in this projection procedure was further minimized. Once the spherical representation was established, standard spherical coordinate systems (e.g., longitude and latitude) were used to index a point on the folded cortical surface for a given subject. Finally, alignment of the cortical surface with a template in the spherical coordinates was implemented by minimizing the mean squared difference between the cortical convexities (Fischl et al., 1999a) of the individual and the template. The spherical mapping in FreeSurfer (v4.0.2) was applied in this study.

CARET cortical mapping

The cortical surface mapping in CARET is a landmark-based spherical registration approach (Van Essen, 2005). To apply it, we first manually delineated six curves, including the central sulcus (CeS), Sylvian fissure (SF), anterior half of the superior temporal gyrus (aSTG), calcarine sulcus (CaS), the medial wall dorsal segment, and the medial wall ventral segment, on the folded cortical surface of each individual subject based on the protocol given on website, http://brainvis.wustl.edu/help/landmarks_core6/landmarks_core6.html. The curves were then projected to the spherical coordinates of the cortical surfaces. Note that the spherical representation of each individual cortical surface was generated using the cortical inflation and spherical projection approaches in FreeSurfer in order to reduce potential errors in evaluation measurements due to different cortical spherical parameterizations. Examples of the curve representation on the sphere are illustrated in Fig. 1(C). Finally, the subject sphere was deformed to the template sphere by forcing the subject landmarks into alignment with the template landmarks and also minimizing local shape distortion of the subject sphere. This landmark-based spherical mapping in CARET (v5.61) was applied in this study.

Quantitative measures of cortical mapping accuracy

Curve variation error

We introduced Hausdorff distance to evaluate anatomical variation based on the local features of the sulcal and gyral curves. For each subject, the 14 sulcal and 12 gyral curves (used in the LDDMM mappings) and six landmarks (used in the CARET mapping) were first transformed to the folded template surface coordinates based on the transformation found using the LDDMM, FreeSurfer, or CARET cortical mapping algorithms. We denoted a specific sulcal/gyral curve of subjects, i and j , in the template coordinates as $\gamma^{(i)}$ and $\gamma^{(j)}$. The Hausdorff distance (Dubuisson and Jain, 1994) was then computed for these paired curves as

$$d(\gamma^{(i)}, \gamma^{(j)}) = 0.5 \frac{1}{N_1} \sum_{x \in \gamma^{(i)}} \min_{y \in \gamma^{(j)}} |x - y| + 0.5 \frac{1}{N_2} \sum_{y \in \gamma^{(j)}} \min_{x \in \gamma^{(i)}} |x - y|$$

where N_1 and N_2 are the number of points on $\gamma^{(i)}$ and $\gamma^{(j)}$, respectively. $|x - y|$ denotes the Euclidean distance between points x and y . The first term in the above equation is the average minimum distance of each point in curve $\gamma^{(i)}$ to a point in curve $\gamma^{(j)}$, and the second term is the average minimum distance of each point in $\gamma^{(j)}$ to a point in $\gamma^{(i)}$.

To evaluate the anatomical variation of a specific sulcal/gyral curve among subjects, which cannot be characterized by the deformation found using the cortical mapping, we further calculated a curve variation error (Pantazis et al., 2010) as

$$\text{Var} = \frac{1}{2J(J-1)} \sum_{i=1}^J \sum_{j=1}^J [d(\gamma^{(i)}, \gamma^{(j)})]^2,$$

where J is the number of subjects in the study. Lower value indicates better alignment for this curve.

Surface alignment consistency and overlap ratio of sulcal regions

Surface alignment consistency (SAC) was initially introduced by Van Essen (2005) for quantifying the anatomical variability of a sulcal region among a group of subjects that can be characterized by the cortical mapping algorithm. Assume J to be the number of subjects involved in the SAC study whose cortical surfaces were transformed to the folded template surface coordinates using the transformation found through one of the cortical mapping algorithms. We considered the region on the template surface that consisted of the sulcal regions transformed from all the J subjects as a reference and denoted its vertex location as x . For every x , we first computed the probability map, $p(x)$, to represent the chance of location x being this sulcal region where $p(x)$ can be approximated as $\frac{j-1}{J-1}$, $i = 1, 2, \dots, J$. We then integrated $p(x)$, over the sulcal region and normalized it by this sulcal area of the template surface. In the discrete case, where the cortical surface was a triangulated mesh, we can define SAC as

$$\text{SAC} = \frac{1}{N} \sum_{i=1}^J \frac{i-1}{J-1} n_i,$$

where N is the total number of vertices in this sulcal region on the template surface and n_i is the number of vertices in this sulcal region with probability of $p(x) = \frac{j-1}{J-1}$. SAC is ranged from 0 to 1, i.e., the higher the value, the better the sulcal alignment.

In our study, one rater (DYL) manually delineated 17 sulcal regions for each of 40 subjects (see detailed protocol in Van Essen, 2005) and on the website (<http://www.bioeng.nus.edu.sg/cfa/mapping/sulcalprotocol.html>). These sulcal regions were chosen because they are distributed broadly over the cortical surface as illustrated in Fig. 3. These sulcal regions were also used for quantifying cortical mapping accuracy in previous studies (Van Essen, 2005). We computed SAC for each of these 17 sulcal regions. To test the intra-reliability of the manual delineation of each region within a subject for ensuring that SAC results were not influenced by the delineation error, the 17 sulcal regions of five subjects were delineated twice (rater: DYL). The second delineation was done three weeks after the first delineation. We computed an overlap ratio for each sulcal region as

$$R = \frac{2N_{S_1 \cap S_2}}{N_{S_1} + N_{S_2}},$$

where $N_{S_1 \cap S_2}$ represents the number of vertices having been labeled as the sulcal region in both manual delineations, while N_{S_i} , $i = 1, 2$ denotes the number of vertices having been labeled as the sulcal region in the i th delineation. Furthermore, the overlap ratio was also computed to quantify the consistency of the sulcal region alignment between individual subjects and the template, where S_1 denoted the sulcal region of the template and S_2 represented the sulcal region of a subject deformed to the template coordinates.

Curvature correlation

The purpose of the cortical surface mapping is to deform one surface to the other such that local and global shape characteristics of the two surfaces are similar. To test it, we computed curvature correlation of the subject's deformed cortical surface and the template

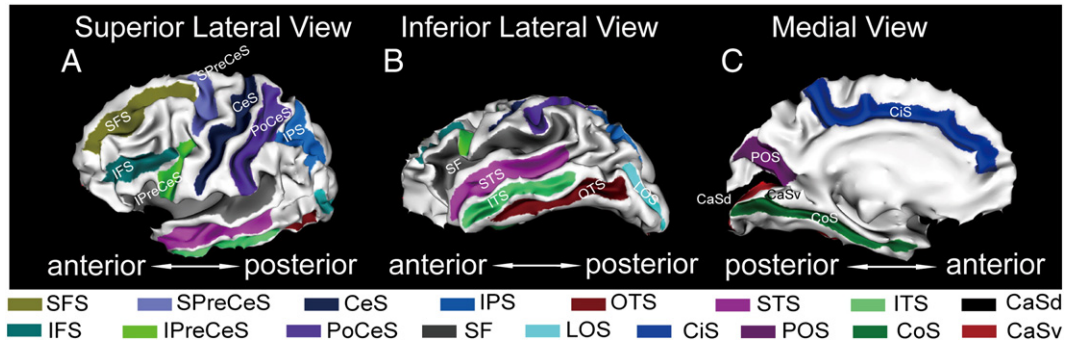


Fig. 3. Seventeen sulcal regions are shown in the superior lateral (A), inferior lateral (B), and medial (C) views of one subject's surface. The names of the sulcal regions are listed in Table 1.

surface. The mean curvature of the subject's deformed surface in the template coordinates was calculated by transferring the mean curvature of the subject folded cortical surface to the template based on the transformation found using one of the cortical mapping algorithms. When $\rho=1$, the global shape pattern of the subject's deformed surface well matches with that of the template surface. The lower value of ρ signals worse registration with a theoretical minimum of $\rho=0$.

Global and local deformation errors

To directly quantify deformation fields that each mapping algorithm characterizes, we conducted a simulation experiment in which folded cortical surfaces were generated from a template by moving its vertices by known deformation. To do this, we modeled deformation, $U(x)$, as random fields in the template coordinates, which can be generated using equation

$$U(x) = \vec{U}_0 + \sum_{i=1}^n U_i \psi_i(x) \vec{N}(x), \quad (2)$$

where \vec{U}_0 is a random vector with three elements. $\vec{N}(x)$ is the normal vector at location x on the template surface. $\psi_i(x)$ is the i^{th} Laplace–Beltrami basis function defined in the template surface (Qiu et al., 2006). Fig. 4 shows examples of the Laplace–Beltrami basis functions on the template surface in the lateral and medial views. The regions with positive values are colored in red, while the ones with negative values are in blue. $\{U_i\}_{i=1}^n$ are random variables associated with $\psi_i(x)$. In our experiment, we used the first 10 Laplace–Beltrami basis functions and applied this model for constructing 10 cortical surfaces from the template where $\{U_i\}_{i=1}^n$ and \vec{U}_0 were randomly generated based on Gaussian distribution. Specifically, $\{U_i\}_{i=1}^n$ and \vec{U}_0 were randomly

chosen such that each individual constructed surface had average deformation displacement across the entire surface about 1–2 mm. Nevertheless, the maximum deformation displacement across the entire surface can be as large as 5.20 mm.

We employed the MM-LDDMM, FreeSurfer, and CARET cortical mapping algorithms to align the 10 individual surfaces to the template. The deformation at a specific location of the cortical surface that cannot be carried out by the mapping algorithms was quantified by the absolute value of the difference between the true deformation obtained in Eq. (2) and deformation fields found through each of the mapping algorithms. We termed it as local deformation error in this paper. The mean value of the local deformation error over the template surface was also computed to give an overall evaluation of the deformation errors, referred to as global deformation error. Since the template was the one used to generate the simulated surfaces, these local and global deformation errors only quantified the amount of deformation that each mapping algorithm can characterize but not the anatomical difference between the template and simulated dataset (e.g., missing gyri or sulci).

Results

We evaluated the accuracy of the LDDMM, FreeSurfer, and CARET cortical mapping algorithms using cortical surfaces of the 40 subjects in the first 3 sections and 10 simulated cortical surfaces in the last section.

Curve variation errors

We computed the variation errors of the 26 curves used in the LDDMM mapping (see Fig. 2) and the 6 curves used in the CARET mapping (see Fig. 1(C)) among the 40 subjects for each of the mapping algorithms. Fig. 5 illustrates these errors to indicate the

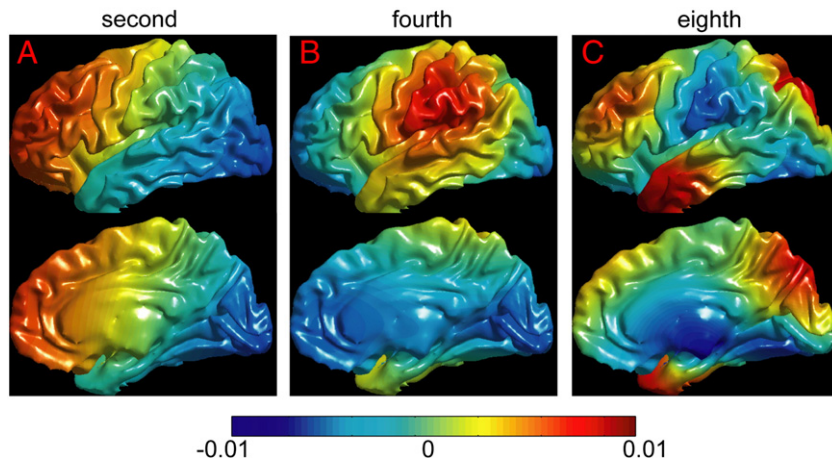


Fig. 4. Panels (A–C) illustrate the second, fourth, eighth Laplace–Beltrami basis functions respectively on the template surface. The top and bottom rows of each panel show the template surface in the lateral and medial views, respectively.

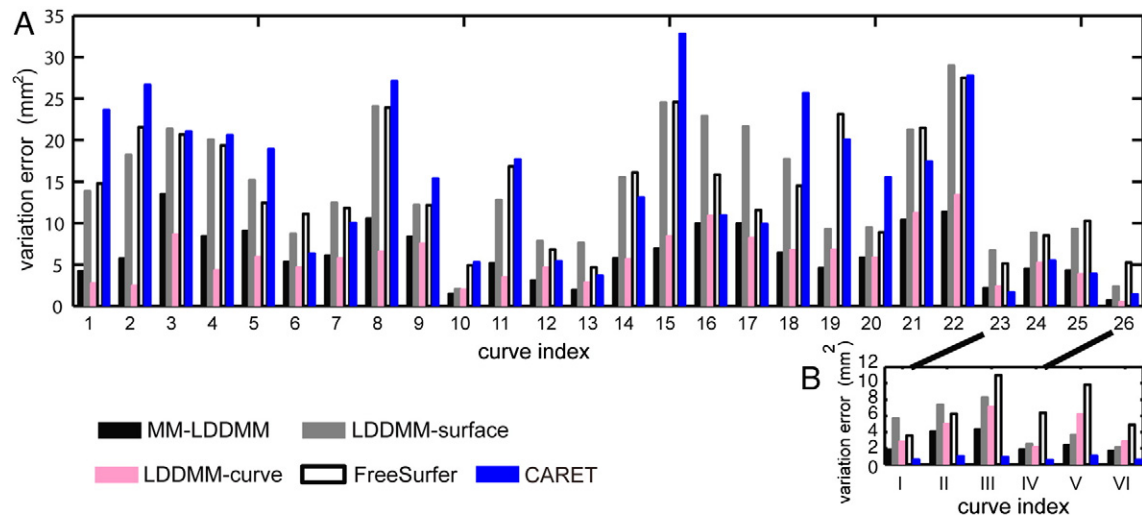


Fig. 5. Panel (A) shows the variation errors of the 26 curves defined for the LDDMM mapping. The full name and index of each curve are given in Fig. 2. Panel (B) illustrates the variation errors of the six curves defined for the CARET mapping, including the central sulcus (I), calcarine sulcus (II), anterior segment of the superior temporal gyrus (III), the medial wall dorsal segment (IV), and the medial wall ventral segment (V), and Sylvian fissure (VI). The first four curves were defined similar to those indexed as 23–26 in panel (A). Black, gray, pink, white, and blue bars are the curve variation errors among 40 subjects that cannot be characterized by MM-LDDMM, LDDMM-surface, LDDMM-curve, FreeSurfer, and CARET cortical mapping algorithms, respectively.

gyral/sulcal variability that cannot be characterized by the deformation found using the LDDMM, FreeSurfer, and CARET mapping algorithms.

As illustrated in Fig. 5(A), the variation errors of the 26 curves suggested that the LDDMM-curve mapping algorithm provided the lowest curve variation errors for most of the 26 curves in comparison to the other mapping algorithms. Compared with FreeSurfer and LDDMM-surface mapping algorithms, the CARET cortical mapping showed relatively lower variation errors of the curves involved in the mapping process, including the central sulcus (index 23), calcarine sulcus (index 24), superior temporal gyrus (index 25), and dorsal segment in the medial wall (close to callosum, index 26), as well as their adjacent curves, including precentral (12) and postcentral (13) gyri, lingual (16) and cuneus (17) gyri. However, the CARET mapping showed larger or comparable variation errors for these curves when compared with the LDDMM-curve mapping. Furthermore, the anatomical variation of the other curves cannot be well carried out using the CARET mapping deformation. In addition, the MM-LDDMM algorithm balanced the geometry of the curves and surfaces when aligning two cortical surfaces. Thus, it provided better curve alignment than the LDDMM-surface, FreeSurfer, and CARET algorithms but had comparable results with the LDDMM-curve algorithm. Overall, the variation errors averaged over all

26 curves were $5.77 (\pm 3.08)$ for LDDMM-curve, $6.36 (\pm 3.31)$ for MM-LDDMM, $14.38 (\pm 6.77)$ for FreeSurfer, $14.41 (\pm 7.17)$ for LDDMM-surface, and $14.89 (\pm 9.19)$ for CARET.

Fig. 5(B) illustrates the variation errors of the six curves defined for the CARET mapping. Our results suggested that CARET provided the lowest variation errors of these six curves when compared with the other mapping algorithms. Notice that among these six curves, four curves (central sulcus, calcarine sulcus, anterior half of the superior temporal gyrus, and the medial wall dorsal segment) were defined similarly to those used for the LDDMM mapping. The variation errors of these four curves from the LDDMM, CARET, and FreeSurfer mappings were comparable with those shown in Fig. 5(A) (curve indices: 23–26). Overall, the variation errors averaged over these six curves were $0.78 (\pm 0.24)$ for CARET, $2.67 (\pm 1.21)$ for MM-LDDMM, $4.33 (\pm 2.05)$ for LDDMM-curve, $4.92 (\pm 2.57)$ for LDDMM-surface, and $6.98 (\pm 2.86)$ for FreeSurfer.

Overlap ratio and surface alignment consistency (SAC)

The second column in Table 1 lists the overlap ratio of two manual delineations of each sulcal region averaged over five subjects. The lowest value of the average overlap ratio was 0.90 for the inferior frontal sulcus while the highest value was 0.96 for the Sylvian fissure.

Table 1

The average overlap ratios (\pm standard deviation, SD) are listed to quantify intra-reliability of the manual sulcal delineation (the second column) and sulcal alignment accuracy of each mapping algorithm (the rest columns).

Sulcal region	Intra-reliability	MM-LDDMM	LDDMM-surface	LDDMM-curve	FreeSurfer	CARET
Central sulcus (CeS)	0.95 ± 0.02	0.63 ± 0.02	0.59 ± 0.05	0.60 ± 0.03	0.63 ± 0.03	0.61 ± 0.02
Parieto-occipital sulcus (POS)	0.95 ± 0.03	0.57 ± 0.06	0.53 ± 0.09	0.54 ± 0.07	0.54 ± 0.08	0.53 ± 0.08
Cingulate sulcus (CiS)	0.94 ± 0.02	0.51 ± 0.05	0.51 ± 0.05	0.49 ± 0.05	0.49 ± 0.05	0.51 ± 0.06
Postcentral sulcus (PoCeS)	0.92 ± 0.04	0.53 ± 0.06	0.49 ± 0.08	0.49 ± 0.06	0.54 ± 0.04	0.51 ± 0.05
Collateral sulcus (CoS)	0.91 ± 0.05	0.46 ± 0.06	0.45 ± 0.05	0.46 ± 0.06	0.47 ± 0.08	0.44 ± 0.06
Superior frontal sulcus (SFS)	0.91 ± 0.02	0.52 ± 0.06	0.52 ± 0.08	0.50 ± 0.06	0.53 ± 0.07	0.52 ± 0.09
Inferior precentral sulcus (IPreCeS)	0.91 ± 0.04	0.47 ± 0.08	0.37 ± 0.13	0.40 ± 0.07	0.39 ± 0.11	0.25 ± 0.11
Superior precentral sulcus (SPreCeS)	0.93 ± 0.02	0.46 ± 0.05	0.47 ± 0.05	0.42 ± 0.06	0.46 ± 0.05	0.49 ± 0.05
Inferior frontal sulcus (IFS)	0.90 ± 0.05	0.37 ± 0.08	0.32 ± 0.08	0.35 ± 0.08	0.35 ± 0.10	0.21 ± 0.12
Inferior temporal sulcus (ITS)	0.91 ± 0.04	0.42 ± 0.10	0.39 ± 0.11	0.38 ± 0.09	0.39 ± 0.10	0.37 ± 0.11
Lateral occipital sulcus (LOS)	0.90 ± 0.04	0.38 ± 0.17	0.34 ± 0.15	0.36 ± 0.15	0.34 ± 0.15	0.38 ± 0.17
Sylvian fissure (SF)	0.96 ± 0.01	0.64 ± 0.02	0.63 ± 0.02	0.56 ± 0.04	0.64 ± 0.02	0.62 ± 0.02
Superior temporal sulcus (STS)	0.92 ± 0.02	0.48 ± 0.05	0.43 ± 0.08	0.39 ± 0.05	0.46 ± 0.06	0.44 ± 0.06
Ventral calcarine sulcus (CaSv)	0.91 ± 0.02	0.46 ± 0.07	0.35 ± 0.12	0.42 ± 0.08	0.41 ± 0.08	0.35 ± 0.09
Dorsal calcarine sulcus (CaSd)	0.91 ± 0.04	0.44 ± 0.08	0.32 ± 0.10	0.42 ± 0.08	0.41 ± 0.09	0.40 ± 0.11
Occipital temporal sulcus (OTS)	0.91 ± 0.06	0.41 ± 0.09	0.41 ± 0.08	0.37 ± 0.08	0.41 ± 0.10	0.44 ± 0.11
Intraparietal sulcus (IPS)	0.92 ± 0.04	0.51 ± 0.05	0.47 ± 0.06	0.44 ± 0.06	0.54 ± 0.06	0.51 ± 0.05

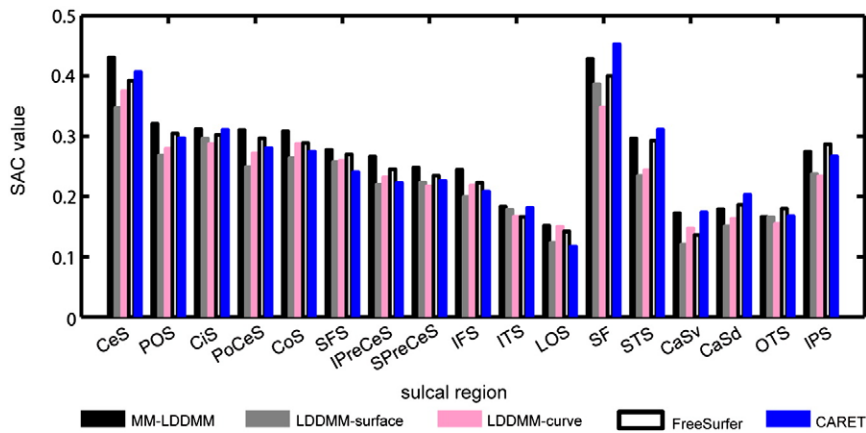


Fig. 6. Surface alignment consistency of the 17 sulcal regions are shown for the MM-LDDMM (black), LDDMM-surface (gray), LDDMM-curve (pink), FreeSurfer (white), and CARET (blue) mapping algorithms. The anatomical definition of each sulcal region is illustrated in Fig. 3. The structural names are listed in Table 1.

The average overlap ratio is above 0.90 for all 17 sulcal regions. The third to seventh columns in Table 1 list the overlap ratio of each sulcal region averaged over the forty subjects for the MM-LDDMM, LDDMM-surface, LDDMM-curve, FreeSurfer, and CARET mappings, respectively. Regardless of the mapping algorithms, both the central sulcal region and Sylvian fissure had higher overlap ratios (ranged from 0.56 to 0.64) than other sulcal regions, while the lateral occipital and inferior frontal sulcal regions had lower overlap ratios (ranged from 0.21 to 0.38) than others. This was consistent with the intra-reliability of the manual delineation, which thus explained that the mapping accuracy was dependent on the variability of anatomical regions across subjects. Overall, the average overlap ratios across the 17 sulcal regions were $0.49(\pm 0.08)$ for MM-LDDMM, $0.45(\pm 0.09)$ for LDDMM-surface, $0.45(\pm 0.07)$ for LDDMM-curve, $0.47(\pm 0.09)$ for FreeSurfer, and $0.45(\pm 0.11)$ for CARET. One sample Student's *t*-tests revealed that the average overlap ratio was significantly decreased in the order of the MM-LDDMM, FreeSurfer, and CARET mapping algorithms (MM-LDDMM vs. FreeSurfer: $p = 0.0084$; FreeSurfer vs. CARET: $p = 0.0355$). The LDDMM-surface, LDDMM-curve, and CARET performed equivalently in terms of this overlap ratio.

Fig. 6 shows SAC measures of each individual sulcal region for the MM-LDDMM (black), LDDMM-surface (gray), LDDMM-curve (pink), FreeSurfer (white), and CARET (blue) mapping algorithms. Regardless of the mapping algorithms, both the central sulcal region and Sylvian fissure had higher SAC values (ranged from 0.35 to 0.45) than other sulcal regions, while the lateral occipital sulcal region had the lowest SAC values (around 0.15). This suggested that the mapping accuracy was highly dependent on the intrinsic anatomical variability of the region. Again, the landmark-based mapping (LDDMM-curve and CARET) provided higher SAC values in the regions where the landmarks were placed. For instance, CARET provided the best alignment in the regions of the Sylvian fissure and superior temporal sulcus. Compared to the LDDMM-surface, the LDDMM-curve had higher SAC values in the regions of the central sulcus, parieto-occipital fissure, postcentral sulcus and so on. Nevertheless, among the three LDDMM mapping algorithms, the MM-LDDMM consistently gave better alignments for all 17 sulcal regions, suggesting that the MM-LDDMM algorithms aligned the local shapes of the cortex well. The SAC for MM-LDDMM was larger than that for FreeSurfer in 14 out of total 17 sulcal regions except the occipital temporal sulcus, the intraparietal sulcus and the dorsal bank of the calcarine sulcus. The SAC for MM-LDDMM was higher than that for CARET in 12 out of total 17 sulcal regions except the dorsal and ventral banks of the calcarine sulcus, the occipital temporal sulcus, the Sylvian fissure, and the superior temporal sulcus that involved or were closed to the landmarks in the CARET mapping. Overall, the SAC values averaged across the 17 sulcal regions were $0.27(\pm 0.08)$ for MM-LDDMM, $0.26(\pm 0.08)$ for FreeSurfer, $0.25(\pm 0.09)$ for CARET, $0.24(\pm 0.07)$ for

LDDMM-curve and $0.23(\pm 0.07)$ for LDDMM-surface. One sample Student's *t*-tests revealed that SAC for MM-LDDMM was significantly higher than FreeSurfer and CARET (MM-LDDMM vs. FreeSurfer: $p = 0.0011$; MM-LDDMM vs. CARET: $p = 0.0107$). The FreeSurfer and CARET mappings performed equivalently in terms of the SAC value. This conclusion was in line with that obtained using the overlap ratio of the sulcal regions.

Curvature correlation

Fig. 7 shows the mean and standard deviation of the curvature correlation between the template and deformed subject surfaces among the 40 subjects. The Student's *t*-tests on the correlation scores of the 40 subjects revealed the decreasing accuracy of the curvature pattern alignment in the order of the MM-LDDMM, LDDMM-surface, LDDMM-curve, FreeSurfer, and CARET mapping algorithms (MM-LDDMM vs. LDDMM-surface: $p < 0.0001$; LDDMM-surface vs. LDDMM-curve: $p < 0.0001$; LDDMM-curve vs. FreeSurfer: $p < 0.0001$; FreeSurfer vs. CARET: $p < 0.0001$).

Local and global deformation errors

We quantified how much deformation can be carried out by the MM-LDDMM, FreeSurfer, and CARET mapping algorithms using the 10 simulated cortical surfaces whose deformation fields relative to the template surface were known. Fig. 8(A, B) illustrates two simulated surfaces colored by their true deformation displacement relative to the template surface. The MM-LDDMM, FreeSurfer, and CARET mapping algorithms were directly applied to align these simulated surfaces to the template. Fig. 8(C–H) shows the deformation displacements carried by the three algorithms. Fig. 9 illustrates local deformation error maps

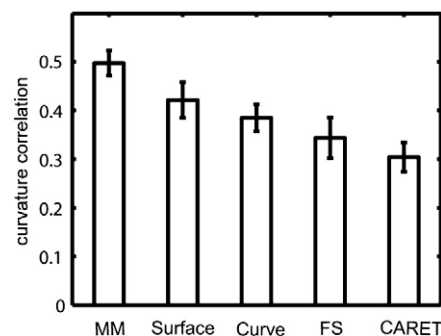


Fig. 7. Bar plot of curvature correlation for the MM-LDDMM (MM), LDDMM-surface (Surface), LDDMM-curve (Curve), FreeSurfer (FS), and CARET mapping algorithms.

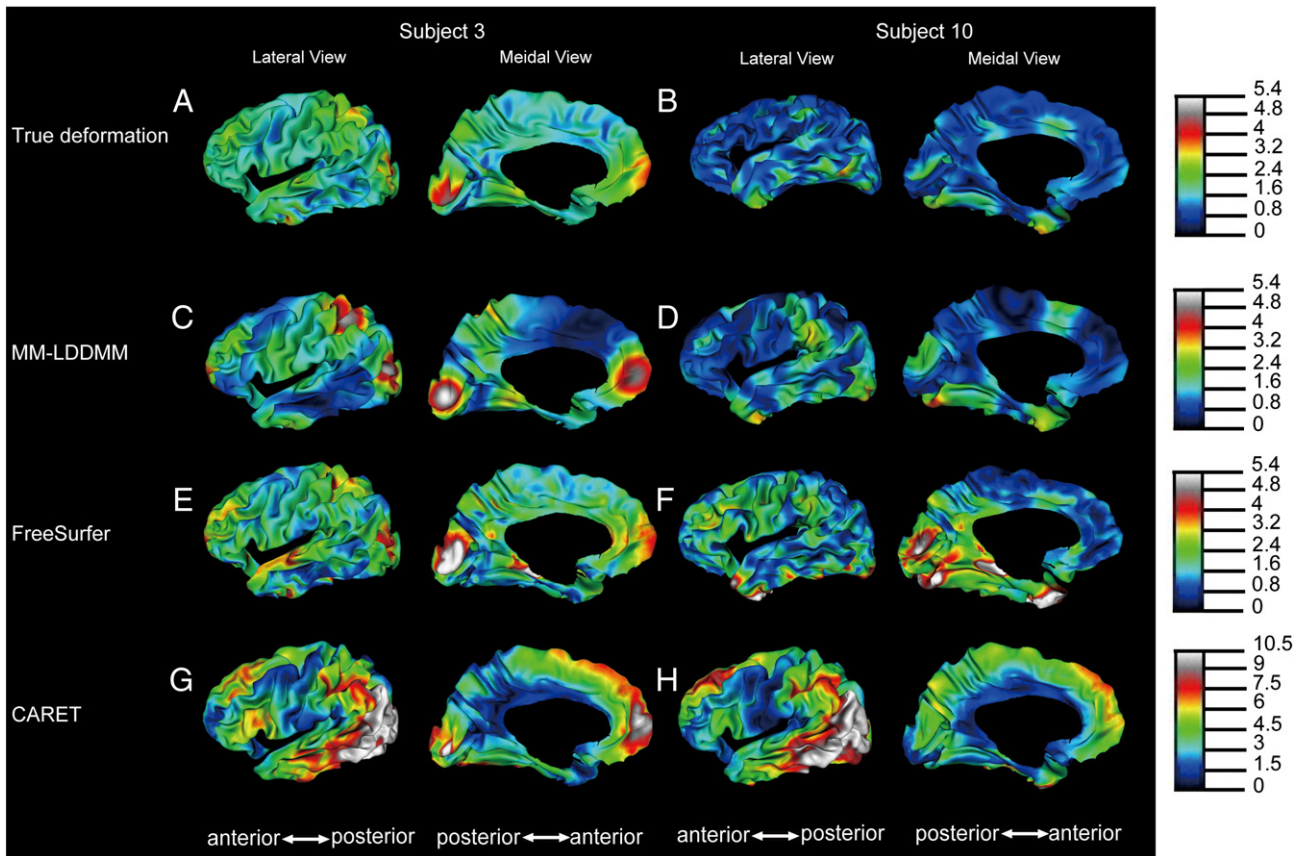


Fig. 8. Left and right panels show two simulated surfaces colored by deformation displacements of the ground truth (A, B), MM-LDDMM (C, D), FreeSurfer (E, F), and CARET (G, H) relative to the template surface. Each cortical surface is illustrated in both lateral and medial views.

averaged over the 10 simulated datasets and their distribution for each of the mapping algorithms. This figure indicates that the MM-LDDMM mapping algorithm had the local deformation errors across the entire surface ranged from 0.35 to 1.93 mm. 74.4% of vertices had the local deformation errors that were less than 1 mm, which is the resolution of MR images. Furthermore, the local deformation errors were relatively uniformly distributed over the surface with the exception of the posterior parietal region. For FreeSurfer, the local deformation errors ranged from 0.43 to 8.74 mm. 35.5% of vertices had the local deformation errors that were less than 1 mm. Large deformation errors were most apparent in the inferio-medial aspect of the frontal lobe, the inferior region of the temporal lobe, and the occipital lobe. For CARET, the local deformation errors ranged from 0.35 to 16.16 mm. 2.85% of vertices had the local deformation errors that were less than 1 mm. Small deformation errors occurred in regions adjacent to the curve landmarks involved in the mapping process. Large deformation errors were most pronounced in the superior regions of the frontal lobe, the inferior region of the temporal lobe, and the lateral aspect of occipital lobe. Overall, average global deformation errors across the 10 simulated data are respectively $0.87 (\pm 0.14)$, $1.20 (\pm 0.15)$, and $4.21 (\pm 0.21)$ for the MM-LDDMM, FreeSurfer, and CARET cortical mapping algorithms, respectively. Student's *t*-tests on global deformation errors of the 10 simulated datasets revealed the MM-LDDMM, FreeSurfer, and CARET mapping algorithms were ranked as decreasing order in terms of their alignment accuracy (MM-LDDMM vs. FreeSurfer: $p = 0.0006$; FreeSurfer vs. CARET: $p < 0.0001$).

Discussion

We quantitatively evaluated the accuracy of the five cortical surface mapping algorithms (MM-LDDMM, LDDMM-surface, LDDMM-curve, FreeSurfer, and CARET) using the 40 MRI scans and 10 simulated

datasets. We computed the curve variation error, overlap ratio of sulcal regions, and surface alignment consistency for assessing the mapping accuracy of local cortical features and the curvature correlation for measuring the mapping accuracy in terms of overall cortical shape. Furthermore, the simulated datasets facilitated the investigation of mapping error distribution over the cortical surface when the MM-LDDMM, FreeSurfer, and CARET mapping algorithms were applied. Our results revealed that the LDDMM-curve, MM-LDDMM, and CARET approaches best aligned the local curve features involved in these mapping algorithms. The MM-LDDMM approach best aligned the local regions and cortical shape patterns (e.g., curvature) as compared to the other mapping approaches. The simulation experiment also revealed that the MM-LDDMM mapping had less local and global deformation errors than the CARET and FreeSurfer mappings. The deformation errors in the MM-LDDMM mapping were relatively uniformly distributed over the surface, but they were not apparent in the same manner in the CARET and FreeSurfer mappings.

Among the five mapping algorithms, LDDMM-curve and CARET registered cortical surfaces based on gyral/sulcal curves, while FreeSurfer and LDDMM-surface aligned cortical surfaces based on features or geometry of the entire cortical surface. As expected, our study showed that the LDDMM-curve and CARET mappings well characterized curve anatomical variations and regions adjacent to landmarks when compared to the FreeSurfer and LDDMM-surface. Thus, LDDMM-curve and CARET can be suggested as the suitable methods in studies on anatomical variations of curves and sulcal regions as well as functional or anatomical studies in specific ROIs (Desai et al., 2005; Qiu et al., 2008). FreeSurfer and LDDMM-surface mapping algorithms may be more appropriate for cortical parcellation when anatomical priors are not available and for whole brain exploratory studies. Nevertheless, statistical outcomes from group studies using these methods may be spurious and dependent on the pattern of the deformation errors as

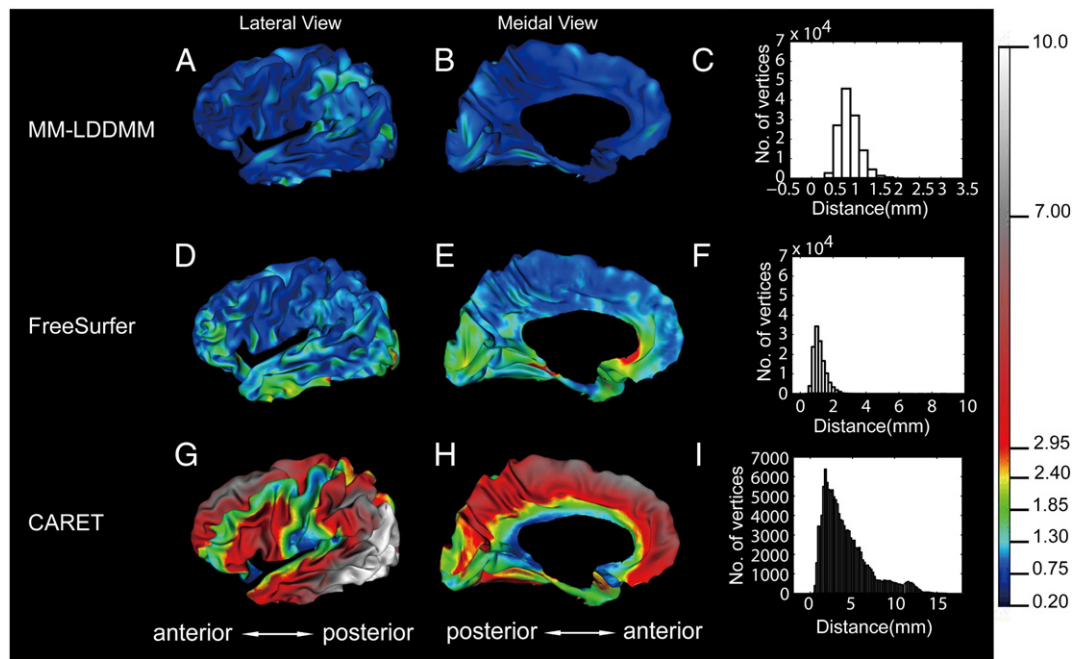


Fig. 9. The local deformation error maps averaged over the 10 simulated cortical surfaces and their distributions are shown for the MM-LDDMM (A–C), FreeSurfer (D–F), and CARET (G–I).

those illustrated in Fig. 9. This can be overcome by introducing weight functions into the FreeSurfer and LDDMM-surface algorithms, where weight functions are defined by adapting regionally specific anatomical variations obtained from postmortem studies (Fischl et al., 2008). The MM-LDDMM algorithm was a more advanced technique that takes advantage of the strengths of both the landmark-based and surface-based cortical mapping approaches by incorporating anatomical priors and minimizing dissimilarity of cortical shape patterns. As automated methods for gyral/sulcal curve delineation (Mangin et al., 2004; Kao et al., 2007) are made available, the MM-LDDMM mapping will be easily used for mapping cortical surfaces in a variety of studies.

In this paper, we classified the mapping algorithms in FreeSurfer and CARET as the spherical-based approaches and the LDDMM algorithms as native-space based approaches. Our results showed that the LDDMM-curve mapping accuracy was comparable to that of the CARET mapping and the LDDMM-surface mapping provided comparable alignments to the FreeSurfer in terms of the curve variation errors, SAC, and curvature correlation. Nevertheless, the MM-LDDMM mapping provided better alignment of the sulcal regions when compared with FreeSurfer and CARET, suggesting that a prior anatomical knowledge (e.g., curves) provided the mapping guidance in the MM-LDDMM algorithm and thus resulted in the good alignment in regions where the anatomical information was defined. In addition, the MM-LDDMM mapping had more uniform deformation errors when compared with FreeSurfer and CARET. The evidence may imply that warping cortical surfaces in their own native folded space in general produced comparable or potentially better alignments as that in the spherical space. One reason could be due to the distortion introduced during the surface parameterization. Further investigation is needed to evaluate influence of the surface parameterization on the cortical alignment.

The quantitative measurements (curve variation errors, SAC, and curvature correlation) involved in our study have been previously examined in several existing studies for assessing and evaluating landmark-based and surface-based cortical surface registrations (Desai et al., 2005; Van Essen, 2005; Pantazis et al., 2010). We chose these measurements because they were commonly used and can become standard measures for evaluating accuracy of cortical surface mapping algorithms. Moreover, they can quantify mapping accuracy from the

aspects of both local (gyral/sulcal curves and sulcal regions) and global (curvature pattern) anatomical features. Using these measures allowed us to compare our study with previous studies and extend our findings to other mapping algorithms that we did not investigate in this study. Pantazis et al. (2010) suggested that the FreeSurfer mapping was better than the landmark-based approach (Joshi et al., 2007) and Brainvoyager (version 1.9.10) (Goebel et al., 2006) in terms of curvature correlation. Taking the above into consideration with our findings, the LDDMM mapping algorithms were likely to also provide better alignment than the landmark-based approach (Joshi et al., 2007) and Brainvoyager (Goebel et al., 2006). Furthermore, Van Essen (Van Essen, 2005) computed SAC of 18 sulcal regions for the CARET mapping. These sulcal regions were all included in our study, with the exception of the middle frontal sulcus which we cannot reliably delineate. Our results for the CARET mapping were consistent with those in Van Essen (2005) according to the SAC distribution across the sulcal regions, i.e., high SAC values in the Sylvian fissure and central sulcal regions and low SAC values in the lateral occipital sulcal region. However, SAC values in our study for each sulcal region were lower than those reported in Van Essen (2005), which may be because MRI scans used in our study were from healthy subjects in a wide age range (20–80 years old) and dementia subjects while MRI volumes of only young healthy adults (18–24 years old) were incorporated in Van Essen (2005). To ensure that the SAC value was reasonable when compared with that reported in Van Essen (2005), we recalculated it for the CARET mapping based on the 10 young subjects in our study. The averaged SAC value across the 17 sulcal regions was 0.29 for the CARET mapping, while it was 0.34 in Van Essen (2005). This discrepancy could be due to the difference in templates. In Van Essen (2005), the average template was created using the same subjects as those in the validation. However, a single-subject template was used in our study, which could potentially increase mapping errors. The average template was not able to be used in our study since the evaluation of the cortical surface alignment may be biased to the mapping algorithm for the template construction.

We have made all datasets, including MRI scans, manually delineated curves and sulcal regions, and simulated surfaces, available online (<http://www.bioeng.nus.edu.sg/cfa/mapping/index.html>) for researchers' further investigation.

Acknowledgments

This study was supported by the National University of Singapore start-up grant R-397-000-058-133, A*STAR SERC 082-101-0025, A*STAR SICS-09/1/1/001.

References

- Anticevic, A., Dierker, D.L., Gillespie, S.K., Repovs, G., Csernansky, J.G., Van Essen, D.C., Barch, D.M., 2008. Comparing surface-based and volume-based analyses of functional neuroimaging data in patients with schizophrenia. *Neuroimage* 41, 835–848.
- Chung, M.K., Robbins, S.M., Dalton, K.M., Davidson, R.J., Alexander, A.L., Evans, A.C., 2005. Cortical thickness analysis in autism with heat kernel smoothing. *Neuroimage* 25, 1256–1265.
- Clouchoux, C., Coulon, O., Riviere, D., Cachia, A., Mangin, J.F., Regis, J., 2005. Anatomically constrained surface parameterization for cortical localization. *Med. Image Comput. Comput. Assist. Interv.* 8, 344–351.
- Dale, A.M., Fischl, B., Sereno, M.I., 1999. Cortical surface-based analysis: I. Segmentation and surface reconstruction. *Neuroimage* 9, 179–194.
- Desai, R., Liebenthal, E., Possing, E.T., Waldron, E.R., Binder, J., 2005. Volumetric vs. surface-based alignment for localization of auditory cortex activation. *Neuroimage* 26, 1019–1029.
- Dubuisson, M.-P., Jain, A., 1994. A modified Hausdorff distance for object matching. *Proceedings of the 12th IAPR International Conference on Computer Vision and Image Processing*, 1, pp. 566–568.
- Fischl, B., Sereno, M.I., Dale, A.M., 1999a. Cortical surface-based analysis. II: Inflation, flattening, and a surface-based coordinate system. *Neuroimage* 9, 195–207.
- Fischl, B., Sereno, M.I., Tootell, R.B., Dale, A.M., 1999b. High-resolution intersubject averaging and a coordinate system for the cortical surface. *Hum. Brain Mapp.* 8, 272–284.
- Fischl, B., Dale, A.M., 2000. Measuring the thickness of the human cerebral cortex from magnetic resonance images. *Proc. Natl. Acad. Sci. U. S. A.* 97, 11050–11055.
- Fischl, B., Salat, D.H., Busa, E., Albert, M., Dieterich, M., Haselgrove, C., Kouwe, A., Killiany, R., Kennedy, D., Klaveness, S., Montillo, A., Makris, N., Rosen, B., Dale, A.M., 2002. Whole brain segmentation: neurotechnique automated labeling of neuro-anatomical structures in the human brain. *Neuron* 33, 341–355.
- Fischl, B., van der Kouwe, A., Destrieux, C., Halgren, E., Segonne, F., Salat, D.H., Busa, E., Seidman, L.J., Goldstein, J., Kennedy, D., Caviness, V., Makris, N., Rosen, B., Dale, A.M., 2004. Automatically parcellating the human cerebral cortex. *Cereb. Cortex* 14, 11–22.
- Fischl, B., Rajendran, N., Busa, E., Augustinack, J., Hinds, O., Yeo, B.T., Mohlberg, H., Amunts, K., Zilles, K., 2008. Cortical folding patterns and predicting cytoarchitecture. *Cereb. Cortex* 18, 1973–1980.
- Glaunès, J., Qiu, A., Miller, M.I., Younes, L., 2008. Large deformation diffeomorphic metric curve mapping. *International Journal of Computer Vision* 80, 317–336.
- Goebel, R., Esposito, F., Formisano, E., 2006. Analysis of functional image analysis contest (FIAC) data with brainvoyager QX: from single-subject to cortically aligned group general linear model analysis and self-organizing group independent component analysis. *Hum. Brain Mapp.* 27, 392–401.
- Gu, X., Wang, Y., Chan, T.F., Thompson, P.M., Yau, S.T., 2004. Genus zero surface conformal mapping and its application to brain surface mapping. *IEEE Trans. Med. Imaging* 23, 949–958.
- Hurdal, M.K., Stephenson, K., 2004. Cortical cartography using the discrete conformal approach of circle packings. *Neuroimage* 23 (Suppl 1), S119–S128.
- Joshi, A.A., Shattuck, D.W., Thompson, P.M., Leahy, R.M., 2007. Surface-constrained volumetric brain registration using harmonic mappings. *IEEE Trans. Med. Imaging* 26, 1657–1669.
- Kao, C.Y., Hofer, M., Sapiro, G., Stem, J., Rehm, K., Rottenberg, D.A., 2007. A geometric method for automatic extraction of sulcal fundi. *IEEE Trans. Med. Imaging* 26, 530–540.
- Lyttelton, O., Boucher, M., Robbins, S., Evans, A., 2007. An unbiased iterative group registration template for cortical surface analysis. *Neuroimage* 34, 1535–1544.
- Mangin, J.F., Riviere, D., Cachia, A., Duchesnay, E., Cointepas, Y., Papadopoulos-Orfanos, D., Scifo, P., Ochiai, T., Brunelle, F., Regis, J., 2004. A framework to study the cortical folding patterns. *Neuroimage* 23 (Suppl 1), S129–S138.
- Marcus, D.S., Wang, T.H., Parker, J., Csernansky, J.G., Morris, J.C., Buckner, R.L., 2007. Open Access Series of Imaging Studies (OASIS): cross-sectional MRI data in young, middle aged, nondemented, and demented older adults. *J. Cogn. Neurosci.* 19, 1498–1507.
- Narr, K.L., Bilder, R.M., Luders, E., Thompson, P.M., Woods, R.P., Robinson, D., Szeszko, P.R., Dimtcheva, T., Gurbani, M., Toga, A.W., 2007. Asymmetries of cortical shape: effects of handedness, sex and schizophrenia. *Neuroimage* 34, 939–948.
- Pantazis, D., Joshi, A., Jiang, J., Shattuck, D., Bernstein, L.E., Damasio, H., Leahy, R.M., 2010. Comparison of landmark-based and automatic methods for cortical surface registration. *Neuroimage* 49 (3), 2479–2493.
- Qiu, A., Bitouk, D., Miller, M.I., 2006. Smooth functional and structural maps on the neocortex via orthonormal bases of the Laplace-Beltrami operator. *IEEE Trans. Med. Imaging* 25, 1296–1306.
- Qiu, A., Miller, M.I., 2007. Cortical hemisphere registration via large deformation diffeomorphic metric curve mapping. *Med. Image Comput. Comput. Assist. Interv. Int. Conf. Med. Image Comput. Comput. Assist. Interv.* 10, 186–193.
- Qiu, A., Younes, L., Wang, L., Ratnanather, J.T., Gillespie, S.K., Kaplan, G., Csernansky, J., Miller, M.I., 2007. Combining anatomical manifold information via diffeomorphic metric mappings for studying cortical thinning of the cingulate gyrus in schizophrenia. *Neuroimage* 37, 821–833.
- Qiu, A., Vaillant, M., Barta, P., Ratnanather, J.T., Miller, M.I., 2008. Region-of-interest-based analysis with application of cortical thickness variation of left planum temporale in schizophrenia and psychotic bipolar disorder. *Hum. Brain Mapp.* 29, 973–985.
- Ratnanather, J.T., Barta, P.E., Honeycutt, N.A., Lee, N., Morris, N.C., Dziorny, A.C., Hurdal, M.K., Pearlson, G.D., Miller, M.I., 2003. Dynamic programming generation of boundaries of local coordinatized submanifolds in the neocortex: application to the planum temporale. *Neuroimage* 20, 359–377.
- Robbins, S., Evans, A.C., Collins, D.L., Whitesides, S., 2004. Tuning and comparing spatial normalization methods. *Med. Image Anal.* 8, 311–323.
- Sowell, E.R., Peterson, B.S., Thompson, P.M., Welcome, S.E., Henkenius, A.L., Toga, A.W., 2003. Mapping cortical change across the human life span. *Nat. Neurosci.* 6, 309–315.
- Thompson, P., Toga, A.W., 1996. A surface-based technique for warping three-dimensional images of the brain. *IEEE Trans. Med. Imaging* 15, 402–417.
- Toro, R., Burnod, Y., 2003. Geometric atlas: modeling the cortex as an organized surface. *Neuroimage* 20, 1468–1484.
- Vaillant, M., Glaunès, J., 2005. Surface matching via currents. *Inf. Process. Med. Imaging, Proceedings* 3565, 381–392.
- Vaillant, M., Qiu, A., Glaunès, J., Miller, M.I., 2007. Diffeomorphic metric surface mapping in subregion of the superior temporal gyrus. *Neuroimage* 34, 1149–1159.
- Van Essen, D.C., Drury, H.A., Joshi, S., Miller, M.I., 1998. Functional and structural mapping of human cerebral cortex: solutions are in the surfaces. *Proc. Natl. Acad. Sci. U. S. A.* 95, 788–795.
- Van Essen, D.C., 2004a. Towards a quantitative, probabilistic neuroanatomy of cerebral cortex. *Cortex* 40, 211–212.
- Van Essen, D.C., 2004b. Surface-based approaches to spatial localization and registration in primate cerebral cortex. *Neuroimage* 23 (Suppl 1), S97–S107.
- Van Essen, D.C., 2005. A population-average, landmark- and surface-based (PALS-B12) atlas of human cerebral cortex. *Neuroimage* 28, 635–662.
- Yeo, B.T., Sabuncu, M.R., Vercauteren, T., Ayache, N., Fischl, B., Golland, P., 2009. Spherical demons: fast diffeomorphic landmark-free surface registration. *IEEE Trans. Med. Imaging* 29, 650–668.
- Zhong, J., Qiu, A., 2010. Multi-manifold diffeomorphic metric mapping for aligning cortical hemispheric surfaces. *Neuroimage* 49, 355–365.